Flow Reversal in Turbulent Boundary Layers with Varying Pressure Gradients

C. Willert[1,*], J. Soria[2], C. Cuvier[3], J.M. Foucaut[3], J.P. Laval[3]

1: DLR Institute of Propulsion Technology, German Aerospace Center, Germany
2: Department of Mechanical and Aerospace Engineering, Monash University (Clayton Campus), VIC 3800, Australia
3: LMFL FRE3723, Univ. Lille, Centrale Lille, CNRS, Villeneuve d'Ascq, France

* Correspondent author: chris.willert@dlr.de

Keywords: turbulent boundary layer, PIV processing, long-range micro PIV, wall shear stress

ABSTRACT

This contribution describes detailed PIV measurements obtained in turbulent boundary layers in an effort to capture rarely occurring flow reversals within the viscous sublayer, which have been observed in both experiments and direct numerical simulations. Due to their confinement to the viscous sublayer along with their rare occurrence on the order of 10^{-4}, any statistical investigation requires very large data sets exceeding 10^5 samples. In the present investigation, this was achieved by capturing long PIV records using image high magnification. To investigate the influence of Reynolds number and pressure gradient, the measurements were performed in turbulent boundary layers in both zero pressure gradient (ZPG) and adverse pressure gradient (APG) conditions. The PIV measurements were performed in the TBL wind tunnel of Lille which features a test section length of 20 m and cross-section of 2 x 1 m^2. A ramp model placed inside the tunnel introduced APG conditions. Both visual inspection of the raw data and a dedicated processing scheme to retrieve the unsteady wall shear stress were used to quantify the flow reversal events. The occurrence of the self-similar flow reversals was found to weakly depend on the Reynolds numbers in ZPG and are roughly doubled in frequency in the APG condition.

1 Introduction

Wall bounded flows submitted to an adverse pressure gradient (APG) are common in many engineering applications, especially in transportation vehicles, such as on the suction side of airfoils. When the strength of the APG is high enough, it can lead to a flow separation, which decreases the performance (increased drag, decreased lift). In the frame of improving the performance of vehicle/aircraft, flow control strategies are tested but most of them try to completely reorganize the flow. At this time, this requires a significant amount of energy which often is not optimal or sometimes even unrealistic. It is therefore important to improve the understanding of the organization of APG flows and to understand the physics of the flow separation which is the basis for new concepts of flow control. The objective of the present investigation is to bring further insights about APG flow organization. In this context, the rare reverse flow events which appear very close to the wall of turbulent boundary layers (TBL) are investigated in detail in order to understand their possible connection with large scale structures which develop in the external region. These events were firstly evidenced by direct numerical

simulations (DNS) of channel flow and zero pressure gradient (ZPG) TBL and was characterized in detail by Lenaers et al. 2012, through a channel flow simulation at low Reynolds numbers. They report a probability of 0.01% at $Re_\tau = 180$ which increases to 0.06% at $Re_\tau = 1000$. They also showed that most of these reverse flow events appear underneath positive large scale region, in agreement with the theory of near wall modulation by large scale structures of Mathis et al. (2009). As the probability of reverse flow events increases also with Reynolds number, this tends to confirm their connection with large scale structures. In APG TBL the large scale structures are found more intense and with a higher frequency of appearance compared to ZPG case (Lee & Sung, 2009). This can be linked with the increasing number of reverse flow events found in APG flows (Vinuesa et al., 2016). As flow separation is defined by a probability of reverse flow events of 50%, understanding their relations with large scale structures can open new ways for flow control strategies, as for example detecting large scale structures responsible of reverse flow events to activate actuators with just the minimum amount of energy to suppress them.

Experimentally, these events are very difficult to measure as it requires high spatial resolution measurements very close to the wall. These structures are 20-40 viscous units in length and remain in the viscous sublayer (Lenaers et al. 2012, Vinuesa et al. 2016). At the same time, very large sample counts are required as their probability is small, typically of the order of 0.1% or less. The existence and topology of reverse flow events and their connection with surrounding flow can nowadays be obtained through particle image velocimetry (PIV) and is chosen for the present investigation.

In the frame of the **EuHIT** project "*Large Scale Structures under Adverse Pressure Gradient*" (Cuvier et al. 2017) which was conducted in the LML wind-tunnel in May 2015, high magnification PIV already provided experimental some evidence of these reverse flow events, however with limited spatial resolution and with small sample counts (Willert et al. 2017). The aim of the present study was to specifically capture the reverse flow events using several different PIV implementations to further understand the underlying mechanisms of their appearance, in particular, under in the influence of different pressure gradients.

A typical example of this flow feature is provided in Fig. 1. In agreement with previous literature on the subject, in particular DNS data, the size of the enclosing zero-velocity streamline of the flow structures is roughly 20-40 wall units in streamwise direction and limited to the viscous sublayer ($y < 5^+$). While difficult to measure, DNS data suggests a spanwise dimension similar to the streamwise extent. The shape of enclosing streamline in the streamwise-wall-normal plane, as indicated by the boundary of the red patch in Fig. 1, was found to be strongly self-similar throughout the acquired data, exhibiting a blunt leading edge and a tapering back end. It should be noted that the DNS typically does not provide this amount of detail.

In Fig. 1 and in the remainder of the text, the streamwise direction is denoted with X, the wall-normal by Y and the spanwise direction by Z. Finally, a superscript '+' denotes scaling in viscous

units $l^* = \nu/u_\tau$ where ν is the kinematic viscosity of air and u_τ is the friction velocity defined as $u_\tau = (\nu\, \partial x/\partial y|_0)^{0.5}$. Here the velocity gradient $\partial x/\partial y|_0$ is the wall shear rate at the wall at $y = 0$ estimated through a specific particle image analysis described within this contribution.

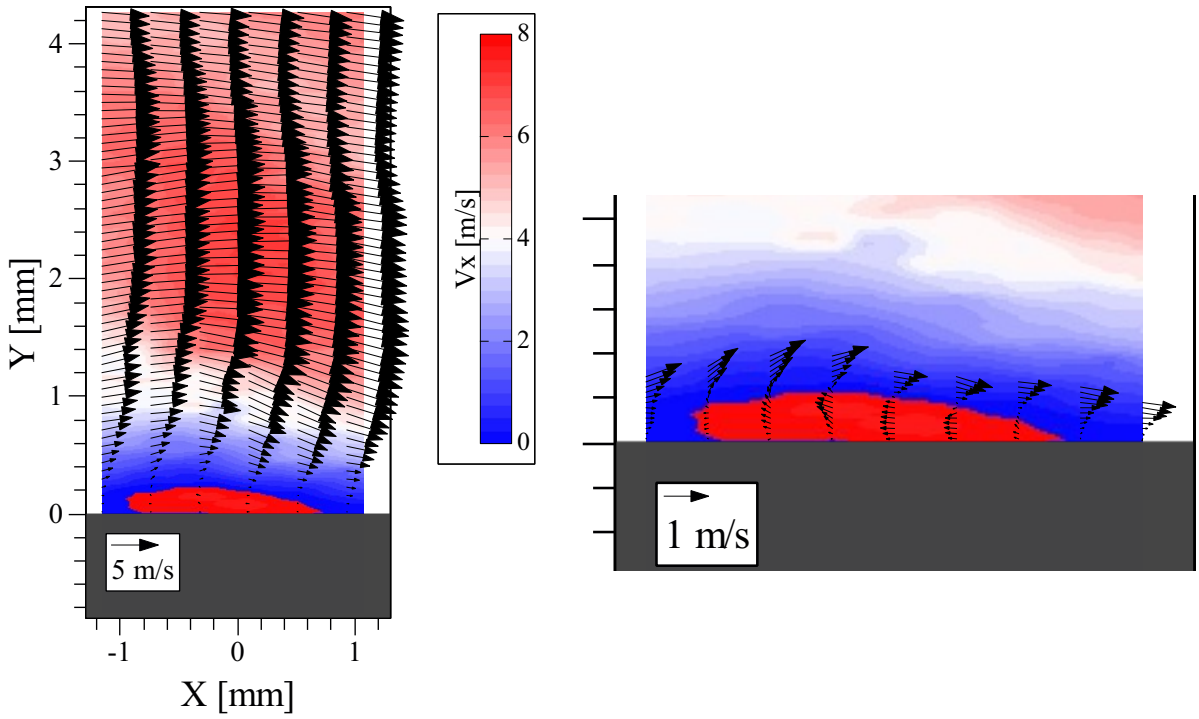

Fig. 1: Single reverse flow event, indicated by the red patch above the wall at $y = 0$ captured in the APGTBL at $U_\infty = 9$ m/s. PIV processing with sampling windows of 24 × 8 pixel ($6.1^+ \times 2.0^+$) with vertical vector spacing of $\delta x = 0.5^+$. The length of the structure is $x = 35^+$, its height $y = 4.5^+$.

2 Experimental methods

2.1 Wind tunnel facility

The measurements are performed in a closed-loop wind tunnel of the LMLF at Centrale Lille which features a test section length of $x = 20$ m with a spanwise width of $z = 2$ m and height $y = 1$ m. Designed for long-duration hotwire measurements, the temperature of the flow is maintained to within ±0.1°C using a heater/chiller system. Measurements are first performed at two streamwise positions (x = 6.8 m and x = 19.2 m) to study the reverse flow with minimal pressure gradient ($\frac{\partial p}{\partial x}^+ \approx -1.4 \times 10^{-4}$ ... -2.0×10^{-4}) at two different free stream velocities. For measurements under the influence of the adverse pressure gradient a ramp is installed in the test section as outlined in Fig. 2. Further details on the facility and the ramp can be found in Cuvier et al. (2018).

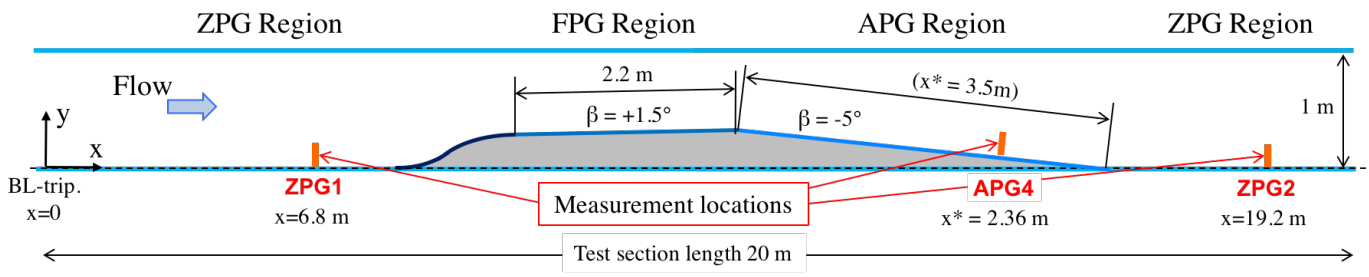

Fig. 2: Wind tunnel test section and measurement locations. Measurements at ZPG2 were performed without installed ramp model.

Table 1: PIV imaging parameters

Measurement location	Sensor area W × H, [pixel]	Imaged area W × H, [mm²]	Pixel pitch [µm]	Image magn. [µm/pixel]	Sample rate
ZPG, APG	224 x 512	2.6 x 6.0	10.0	11.75	10 – 25 kHz
ZPG, x=6.8	200 x 2560	3.3 x 41.5	6.5	16.35	200 Hz

2.2 PIV instrumentation

The current investigation relies on data acquired in a streamwise wall normal plane (XY) using two-component, two-dimensional (2C-2D) particle image velocimetry (PIV). For image recording, a high-speed camera (Miro310, Vision Research) and a sCMOS double-frame PIV camera (Edge5.5, PCO AG) was used. Specifics of the PIV instrumentation are summarized in Table 1.

In spite of the large working distance of more than 1 m, an image magnification m>1.0 was achieved using f=300 mm telephoto lenses (Nikon Nikkor 300/4.0) together with tele-converters (Nikon TC2.1) that double the effective focal lengths to 600 mm with the caveat of reducing the numerical aperture by the same amount. In addition, the aperture of the lenses had to be stepped down by at least one more f-stop to $f_{\#,\mathrm{eff}} = 11$ to reduce the diffraction size of the imaged particle (smaller particle images). In order to prevent image diffraction near the glass wall due to a partially occluded lens aperture, the optical axis was inclined by about 1° with respect to the wall.

Using a high-speed laser (NanioAir, Innolas Photonics) the particles were illuminated with a light sheet of about $\delta x = 2$ mm width and thickness of about $\delta z = 200$ µm (as measured with burn paper). The pulse energy at 20 kHz is 0.5 µJ/pulse with a corresponding fluence of about 1.25 µJ/mm^2 and a pulse width on the order of 20 ns.

The wind tunnel was continuously seeded with a water glycol mixture using an evaporation-condensation fogger producing droplets in the range 1-2 µm. The seeding density was estimated from the image data at 3000 particles/mm^3.

2.3 Estimation of the mean and unsteady wall shear stress

The wall shear rate $\partial x/\partial y|_0$ and with it the wall shear stress $\tau_w = \nu\, \rho\, \partial x/\partial y|_0$ is determined from the near-wall, streamwise velocity u obtained through the measurement of particle motion in the image data. The particles are typically in the 1–2 µm range which is more than one order of magnitude smaller than the viscous scales in the flow ($l^* = \nu/u_\tau = 40 - 120$ µm). Given a

conservative particle response time of $t_p \approx 10$ µs or $t_p \approx 0.03\ t^+$ the Stokes number $St = t_p\ U\ d^{-1}$ based on friction velocity u_τ and viscous sublayer thickness $d = 5y^+$ reduces to 0.005, which indicates that the particles follow the flow faithfully.

If sufficient velocity estimates are available from within the viscous sublayer, preferably in the range $0 < y < 3^+$, the velocity gradient can be estimated through finite differences (Willert, 2015). Here it is worth noting that the magnification factor relating physical space to image space is not required since it cancels out in the estimation of the gradient. This makes the measurement approach particularly attractive as it only requires the knowledge of the time separation between the image recordings, Δt.

The near wall velocity can be determined from single lines of wall-parallel pixel rows using one-dimensional cross-correlation. This can be achieved very efficiently by compiling all pixel rows in a common image such as presented in Fig. 3. If the sequence is temporally well resolved, the movement of particles shows up as streaks. The slope of these streaks is a direct indication of their actual velocity as projected onto the pixel row. Movement normal to the pixel row or outside of the light sheet plane results fading or appearing of streaks. Changes in slope indicate acceleration or deceleration.

For the correlation analysis adjacent rows (or separated by one or more rows) are cross-correlated using multiple one-dimensional FFTs performed in parallel. A three-point Gaussian peak fit locates the maximum correlation with sub-pixel accuracy in analogy to conventional 2-C PIV processing. For a continuous image sequence of N images this results in (N-1) velocity estimates for each pixel row above the wall. Along with the data from the other rows the mean velocity profile can be determined and is used to estimate the mean velocity gradient for the image sequence using a linear least squares fit (see e.g. Fig. 4, left). It should be noted that the length of the correlation sample, typically the image width, defines the domain over which the velocity is averaged, so there will be a smoothing influence on the recovered data along the streamwise direction. In spanwise direction the degree of smoothing depends on the light-sheet thickness, which is about 0.2-0.3 mm.

In a second step the unsteady wall shear rate is determined by performing a linear least squares fit using the group of velocity estimates for each time instant. This data can then be used to provide statistical estimates of the wall shear stress, such as its RMS, skew and flatness (kurtosis). Normalized probability density functions (PDF's) of the unsteady wall shear stress, such as shown in Fig. 4, right, allow for a visual comparison of the retrieved data for the various flow conditions. Here the logarithmic scaling of the probability axis reveals features such as rarely occurring reverse flow events ($\tau_w < 0$) or very fast streaking events at the other end of the PDF.

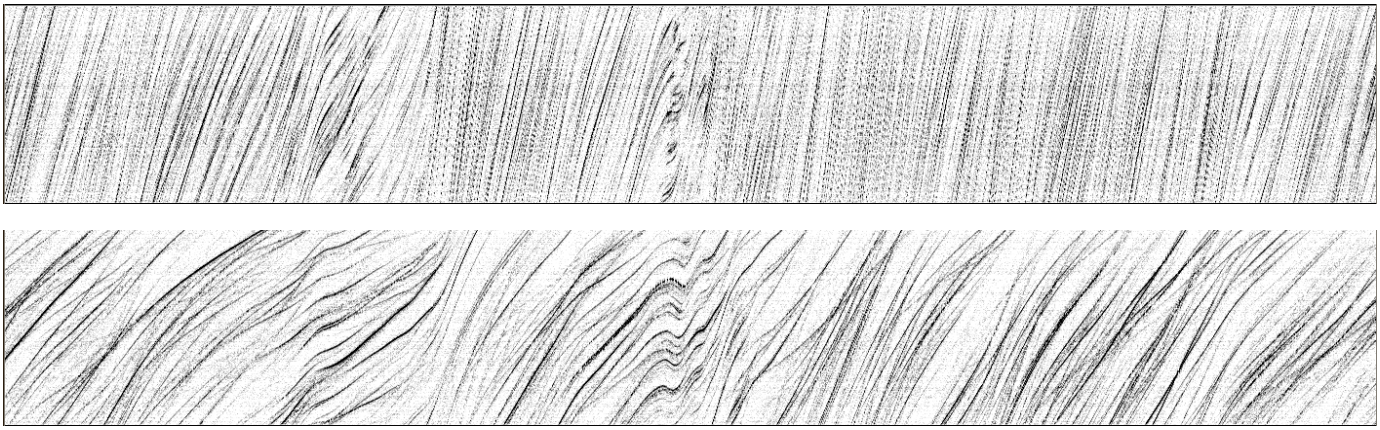

Fig. 3: Particle streak images compiled from high-speed particle image recordings by extracting a fixed row of pixels from each image. The top image is at a wall distance of 180 µm ($4.6y^+$), the lower image at 55 µm ($1.3y^+$). The vertical axis coincides with the streamwise axis X whereas the horizontal axis corresponds to time – here 0.056 s (1400 samples). The signature of a single reverse flow event can be seen near the middle of the images.

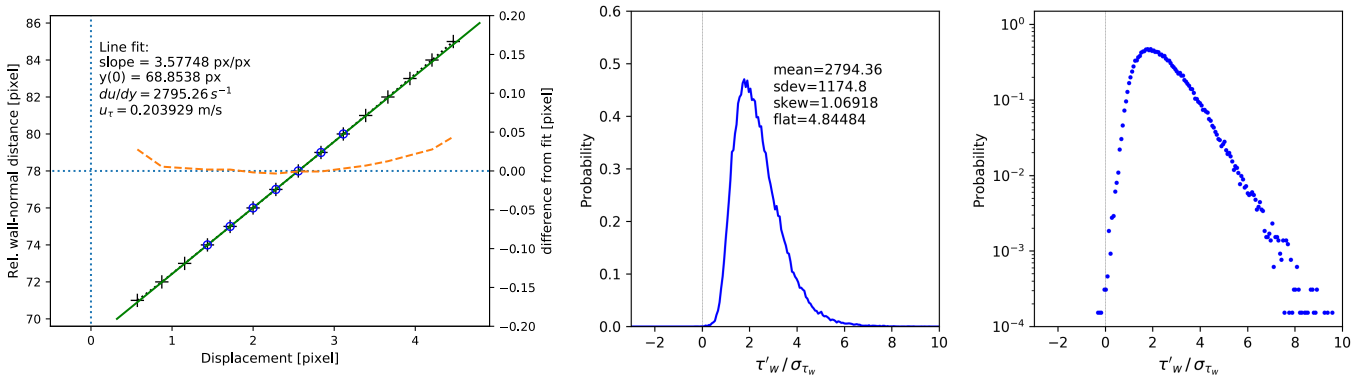

Fig. 4: Left: estimation of the mean velocity gradient from the velocity profile using linear least squares fit. The circled symbols are used for the fit; the orange dashed line shows the deviation from the linear fit. Right: PDF's of the wall shear rate for a single image sequence in linear and linear-logarithmic representation. Values to the left of the vertical line at zero indicate negative shear stress events.

3 Results and discussion

The statistics of the near-wall velocity and related quantities are summarized in Table 2. For the ZPG the higher moments (skew and flatness) and the ratio of the RMS and mean shear rate show no noticeable dependence on Reynolds number. Under the influence of the APG these quantities show a slight increase. The probability density distributions for three relevant flow conditions are shown in Fig. 5 and indicate two aspects: (1) with increasing the Reynolds number the PDF broadens (red vs. blue line), and (2) the adverse pressure gradient broadens the PDF even further. Here the probability of zero and negative wall shear stress increases significantly from about 1×10^{-4} in ZPG to about 1×10^{-3} in APG. An influence of Reynolds number for ZPG conditions cannot be observed as clearly as in the DNS results provided in the literature (e.g. Diaz-Daniel et al. 2017, Örlü & Schlatter 2011).

Table 2: Near-wall velocity statistics

	ZPG, x = 6.8 m		ZPG, x = 19.2 m		APG4, x^* = 2.36 m	
free stream velocity, U_∞	5 m/s	9 m/s	6 m/s	9 m/s	5 m/s	9 m/s
shear velocity, u_τ	0.204 m/s	0.343 m/s	0.232 m/s	0.340 m/s	0.181 m/s	0.322 m/s
viscous length, $l^* = \nu/u_\tau$	73.7 µm	43.7 µm	64.7 µm	44.2 µm	81.9 µm	46.2 µm
Reynolds number, Re_τ	1840	2360	3840	5590	2350	3990
Reynolds number, Re_θ	5620	8120	12720	18360	10630	17700
shear rate, $S = du/dy$	2770 s^{-1}	7860 s^{-1}	3580 s^{-1}	7690 s^{-1}	2220 s^{-1}	6960 s^{-1}
std. deviation, σ_s	1180 s^{-1}	3260 s^{-1}	1490 s^{-1}	3300 s^{-1}	1010 s^{-1}	3250 s^{-1}
ratio, σ_s/S	0.43	0.42	0.42	0.43	0.46	0.47
skew(S)	1.09	1.05	1.04	1.13	1.24	1.20
flatness(S)	5.15	4.66	4.59	4.99	5.52	5.00
samples, N	220,000	400,000	950,000	3,920,000	2,410,000	3,000,000
width of sample domain, Δx	44^+	75^+	41^+	53^+	32^+	57^+

For the estimation of the actual number of reverse flow events, manual scanning of the streak images of the type shown in Fig. 3 was performed. The recovered reverse flow data is summarized in Table 3. The frequency of event occurrence increases both with Reynolds number and under the influence of the adverse pressure gradient. Determining the probability of the reverse flow events from the event counts is must take into account the fact that the data is temporally correlated and requires an estimate of the actual number of independent samples. For the present analysis, the mean temporal spacing t_{rev} of the reverse flow events is normalized with the width of the field of view (Δx ~ 2mm) and the edge velocity U_∞. Based on this estimate, the reverse flow probability approximately doubles under the influence of the APG. An influence of the outer flow velocity on this probability presently cannot be conclusively determined.

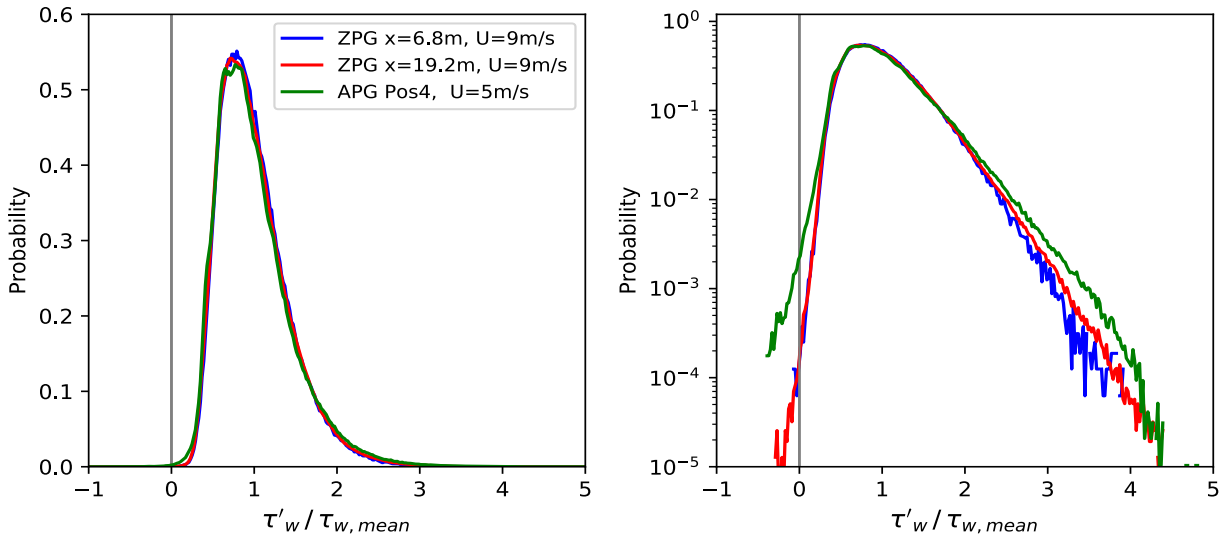

Fig. 5: PDFs of the wall shear stress at streamwise positions x = 6.8 m (Re_τ = 2360, blue), at x = 19.2 m (Re_τ = 5590, red) and in the APG region (green).

Table 3: Statistics of reverse flow events

	ZPG, x = 19.2 m		**APG4, x^* = 2.36 m**	
free stream velocity, U_∞	6 m/s	9 m/s	5 m/s	9 m/s
Reverse flow events	41	219	169	(380)[1]
Number of images, N	952,000	3,920,000	2,410,000	3,000,000
Number of sequences	13	42	33	36
Total sequence duration	47.6 s	157 s	121 s	150 s
Mean temporal event spacing	1.16 s	0.72 s	0.71 s	0.39 s
Mean event spacing in viscous units	4160 t^+	5520 t^+	1560 t^+	2730 t^+
Estimated probability	$2.8\text{x}10^{-4}$	$3.1\text{x}10^{-4}$	$5.6\text{x}10^{-4}$	$5.5\text{x}10^{-4}$

4 Summary and outlook

Over the course of one month a PIV measurement campaign acquired an extensive data base of the near-wall flow of a turbulent boundary layer at both near-zero pressure gradient and adverse (positive) pressure gradient. The number of samples in excess of 10^5 for all conditions studied is believed to be sufficient to allow a more quantitative assessment regarding the statistics of rarely occurring phenomena such as flow reversal. Beyond the high-magnification data presented here, the data base includes measurements at similar magnifications using large format sensors (5.5 MPixel and 29 MPixel) to assess the interaction of reverse flow events in larger areas of interest. Stereoscopic PIV measurements of the spanwise, wall-normal plane at high-magnification and high frame rates obtained in the APG region will allow the investigation of the spanwise flow field surrounding the reverse flow events by the capturing streamwise vorticity field.

The material presented in the previous sections is still subject to further investigation the results of which will be provided in upcoming publications. This will include an assessment of the effects of spatial filtering on the estimation of the unsteady wall shear rate. For instance, the present PDFs given in Fig. 5 do not show APG data at $U_\infty = 9$ m/s due to the presence of spatial filtering artifacts and loss of signal at higher velocities. Also wall vibrations present on the APG ramp amounting to 1-2 wall units so far have not been accounted for and may also contaminate estimates of the wall shear rate. Further topics yet to be recovered from the data base are the comparison of wall shear stress statistics and related power spectra with recently published DNS data, such as by Diaz-Daniel et al. (2017). Finally, the self-similar shape and surrounding flow topology of the reverse flow events will be analyzed based on conditionally averaged flow fields such as performed by Jalalabadi & Sung (2018) on DNS data of a pipe flow.

References

Cuvier C., Srinath S., Stanislas M., Foucaut J. M., Laval J. P., Kähler C. J., et al. (2017). Extensive characterisation of a high Reynolds number decelerating boundary layer using advanced optical metrology. *Journal of Turbulence* 18(10), 929-972. http://doi.org/10.1080/14685248.2017.1342827

Diaz-Daniel C., Laizet S., Vassilicos J. C. (2017). Wall shear stress fluctuations: Mixed scaling and their effects on velocity fluctuations in a turbulent boundary layer. *Physics of Fluids* 29(5), 055102. http://doi.org/10.1063/1.4984002

Eitel-Amor G., Örlü R., Schlatter P. (2014) Simulation and validation of a spatially evolving turbulent boundary layer up to $Re_\theta = 8300$. *International Journal of Heat and Fluid Flow* 47, 57–69 https://doi.org/10.1016/j.ijheatfluidflow.2014.02.006

Jalalabadi R., Sung H. J. (2018). Influence of backflow on skin friction in turbulent pipe flow. *Physics of Fluids* 30(6), 065104–10. http://doi.org/10.1063/1.5026998

Lee J.-H., Sung H. J. 2009 Large scale structure of turbulent boundary layer subjected to an adverse pressure gradient. In *Sixth International Symposium on Turbulence and Shear Flow Phenomena*, pp. 153–158. Seoul, Korea, 22-24 June, 2009.

Lenaers P, Li Q., Brethouwer G., Schlatter P., Örlü R. (2012). Rare backflow and extreme wall-normal velocity fluctuations in near-wall turbulence. *Physics of Fluids* 24, 035110 http://doi.org/10.1063/1.3696304

Mathis R., Hutchins N., Marusic I. (2009). Large-scale amplitude modulation of the small-scale structures in turbulent boundary layers. *Journal of Fluid Mechanics 628*, 311–27. http://doi.org/10.1017/S0022112009006946

Örlü R., Schlatter P. (2011). On the fluctuating wall-shear stress in zero pressure-gradient turbulent boundary layer flows. *Physics of Fluids* 23(2), 021704–5. http://doi.org/10.1063/1.3555191

Sillero J. A., Jimenez J., Moser R. D. (2013). One-point statistics for turbulent wall-bounded flows at Reynolds numbers up to $\delta^+ \approx 2000$. *Physics of Fluids* 25, 105102 http://link.aip.org/link/doi/10.1063/1.4823831

Vinuesa R., Örlü R., Schlatter P. (2016). Characterisation of backflow events over a wing section. *Journal of Turbulence* 18(2), 1–17. http://doi.org/10.1080/14685248.2016.1259626

Willert C. E. (2015). High-speed particle image velocimetry for the efficient measurement of turbulence statistics. *Experiments in Fluids* 56(1), 17–17. http://doi.org/10.1007/s00348-014-1892-4

Willert C., Cuvier C., Foucaut J., Klinner J., Stanislas M., Laval J., Srinath S., Soria J., Amili O., Atkinson C., Kähler C., Scharnowski S., Hain R., Schröder A., Geisler R., Agocs J., Röse A. (2018). Experimental evidence of near-wall reverse flow events in a zero pressure gradient turbulent boundary layer. *Experimental Thermal and Fluid Science* 91, 320–328. https://doi.org/10.1016/j.expthermflusci.2017.10.033